Adaptive Bioinspired Preview Suspension Control With Constrained Velocity Planning for Autonomous Vehicles

Tenglong Huang, Jue Wang, and Huihui Pan, *Senior Member, IEEE*

***Abstract*—Autonomous vehicles equipped with numerous advanced sensors are capable of obtaining road preview information, creating new opportunities for vehicle suspension systems. This article proposes a novel preview suspension control method from adaptive nonlinear control perspectives with less computational burden and is more realistic, unlike optimization-based works or existing linear state-space models-based results that neglected nonlinear terms. The X-shaped bio-inspired dynamics derived from animal or insect skeleton structures are introduced to reduce energy consumption by utilizing beneficial geometrical nonlinearities. Meanwhile, optimal velocity planning approach is investigated to balance vehicle passage time, vibration suppression, and longitudinal comfort by solving a multi-objective optimization problem with the aid of road preview information. Moreover, acceleration constraint reduces the search space and computing requirements, while ensuring planned velocity optimality. Simulation and experiment results are provided to demonstrate the effectiveness and advantages of the constructed energy-saving adaptive preview control framework with constrained velocity planning.**

***Index Terms*—Adaptive preview suspension, autonomous vehicles, bioinspired dynamic, constrained velocity planning, energy-saving.**

I. Introduction

VEHICLE chassis system consists of lateral, longitudinal, and vertical subsystems corresponding to steering, driving/braking, and suspension systems, respectively. The vehicle suspension system [1], [2], [3] plays a crucial role in the performance of ride comfort, thus, making it an active area and has captured considerable attention from researchers. Particularly, autonomous vehicles [4] equipped with various perception sensors, as illustrated in Fig. 1, have powerful sensing capabilities that enable them to obtain road excitation in advance. Connected autonomous vehicles [5], [6], [7], [8] can also obtain sufficient environment information via cloud services or vehicle-to-everything technology by virtue of wireless network communication [9], [10]. This provides new perspectives and opportunities for handling vehicle suspension control problems using road preview information which is the focus of this development. Although related research is emerging, it is still lacking.

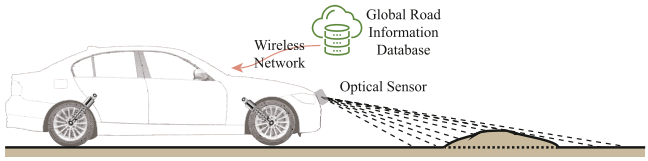

Fig. 1. Autonomous vehicles with road preview information.

There have been few effective attempts to design a preview suspension control scheme in the literature. The front vehicle is taken as preview sensor to construct an optimal controller based on the linear quadratic regulator (LQR) in [11]. The performance improvement of output feedback H_∞/GH_2 control strategy over linear quadratic gaussian preview is validated in [12]. Model predictive control (MPC) provides another feasible solution to this issue. An implicit MPC controller [13] is implemented to illustrate the benefits that come from MPC and preview data by means of experimental results on a high-mobility vehicle, which is compared with the non-preview skyhook damping controller and LQR method. Hybrid MPC with time-varying horizon is utilized to handle the preview information in [14]. MPC incorporated with displacement trajectory optimization utilizing measured road data is adopted in [15], improving ride comfort with fewer optimization variables. To overcome memory and computational burdens, the explicit regionless MPC in [16] employing offline optimization is developed. An adaptive gain scheduling preview controller is realized in [17] by adjusting the gain automatically. Nevertheless, most of the recent emergence of vehicle preview control methodology is optimization-based or uses simplified linear state-space models. Accordingly, the designed controllers present expensive computational burdens or ignore the nonlinear characteristics.

The classical computationally efficient adaptive control method [18] achieves an impressive effect by controlling the sprung mass in conjunction with zero dynamic analysis.

Manuscript received 3 April 2023; revised 29 April 2023; accepted 1 May 2023. Date of publication 8 May 2023; date of current version 21 August 2023. This work was supported in part by the National Natural Science Foundation of China under Grants 62173108, U1964201, and 62022031, in part by the Post-Doctoral Science Foundation under Grants 2019T120270 and LBH-TZ2111, in part by the Major Scientific and Technological Special Project of Heilongjiang Province under Grant 2021ZX05A01, and in part by the Fundamental Research Funds for the Central Universities under Grant HIT.OCEF.2022012. *(Corresponding author: Huihui Pan.)*

Tenglong Huang and Jue Wang are with the Research Institute of Intelligent Control and Systems, Harbin Institute of Technology, Harbin 150001, China (e-mail: huangtenglong@hit.edu.cn; juewang@hit.edu.cn).

Huihui Pan is with the Research Institute of Intelligent Control and Systems, Harbin Institute of Technology, Harbin 150001, China, and also with the Robot Innovation Center Company Ltd., Harbin Institute of Technology, Harbin 150001, China (e-mail: huihuipan@hit.edu.cn).

Color versions of one or more figures in this article are available at https://doi.org/10.1109/TIV.2023.3273620.

Digital Object Identifier 10.1109/TIV.2023.3273620

However, it must be pointed out that road excitation is isolated by the unsprung mass in this approach and is thus no longer applicable for suspension preview control. One viable option is to take suspension space and its derivative as the system state variables. Moreover, another critical issue worth considering for suspensions is energy consumption, especially for active suspensions. In this case, this article attempts to reduce the energy consumption while decreasing the computational burden. To achieve energy savings and provide a reference trajectory, bioinspired dynamics are constructed elaborately and introduced as a reference model. Inspired by the superior vibration isolation achieved by the special structures of bird legs or animal skeletons [19], the study of limb-like anti-vibration structures has been an interesting and hot topic. Scissor-like and X-type [20] bionic structures have been designed and successfully applied to spacecraft, Stewart platform, and underwater robots. It is worth noting that asymmetrical X-shaped structures [21] are effective in isolating vibrations while obtaining excellent energy savings and, more importantly, the stability of the dynamic structure has been proved by the Lyapunov method. Consequently, the bionic dynamics model with an asymmetric X-shaped structure is designed and adopted in this article to optimize ride comfort and energy consumption by exploiting beneficial non-linearities.

Human drivers intuitively slow down to suppress the discomfort caused by a bulge ahead, such as a speed bump, and then accelerate after passing the bulge. Road preview information for autonomous vehicles offers the possibility of mimicking this behavior through longitudinal velocity planning. Nevertheless, frequent acceleration and deceleration have detrimental effects on vehicle performance. Thus, the velocity planning is modeled as a longitudinal and vertical multi-objective optimization problem to strike a balance in this article. In the literature [22], [23], several works have begun to exploit road preview information for path planning, vertical trajectory planning and longitudinal velocity planning [24]. For example, [14] proposes a novel comfort-orient speed planning algorithm, however, it searches the entire speed candidates space, which can easily lead to unreasonable planned speed or require a large adjustment interval. Relevant research is still limited and leaves some room for improvement.

Motivated by the challenges and discussions above, this article proposes an adaptive bioinspired preview suspension control scheme with constrained velocity planning for autonomous vehicles, which offers the following contributions:

1) A constrained velocity planning algorithm is proposed to balance the vertical ride comfort, longitudinal comfort, and passage time. The presented algorithm allows for arbitrary velocity regulation interval and avoids unreasonable or undesired velocity jumps by taking constraints into account. The optimality of the planned velocity trajectory is ensured, and velocity candidates that do not satisfy the constraints are removed from search space, resulting in a reduced computational demand.
2) Based on the planned velocity and road information, this article presents a preview controller employing generated road excitation from an adaptive control perspective. To the authors' knowledge, this study is the first to propose a nonlinear adaptive bionic preview suspension controller that is based on a nonlinear state-space model. The controller is more realistic and has low computational requirements, as no optimization is required.
3) Moreover, the animal limb-inspired bioinspired dynamics are introduced as reference trajectories to take advantage of the beneficial nonlinearities, achieving significant energy savings. The proposed method is deployed to the physical platform, and the simulation and experimental results demonstrate the advantages of this approach.

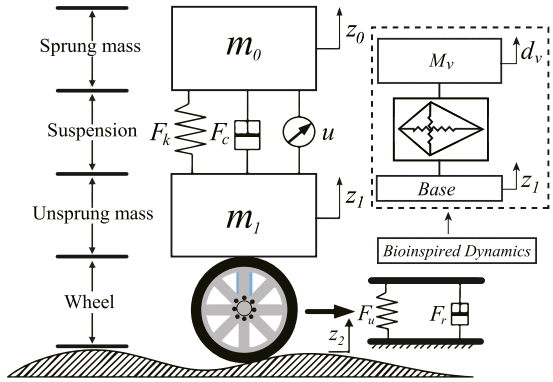

Fig. 2. Quarter-vehicle model.

II. Problem Statement

The quarter vehicle model of active suspension and constrained multi-objective optimization problem are stated in this section. Additionally, quantitative performance indicators are introduced.

A. Active Suspension Mathematical Model

As shown in Fig. 2, the active suspension [25], [26] can be described as a two-degrees-freedom spring-damper system. The weights of vehicle body and wheel are considered as sprung mass m_0 and unsprung mass m_1, respectively. The vertical displacements of m_0 and m_1 are represented as z_0 and z_1 with road surface height z_2. F_k and F_c denote the forces produced by the nonlinear spring and damper of suspension. The spring and damper forces for wheel tire are described as F_u and F_r. And u is the control input produced by electric actuator. Based on Newton's law and the mechanical characteristics of spring and damper, the vertical dynamics of vehicle body motion and unsprung mass can be derived as follow

$$m_0\ddot{z}_0 = -F_k(z_0, z_1) - F_c(\dot{z}_0, \dot{z}_1) + u(t) \tag{1}$$

$$m_1\ddot{z}_1 = F_k(z_0, z_1) + F_c(\dot{z}_0, \dot{z}_1) - F_u(z_1, z_2) - F_r(\dot{z}_1, \dot{z}_2) - u(t) \tag{2}$$

where

$$F_c(\dot{z}_0, \dot{z}_1) = k_{c1}(\dot{z}_0 - \dot{z}_1) + k_{c2}(\dot{z}_0 - \dot{z}_1)^2$$

$$F_k(z_0, z_1) = k_m(z_0 - z_1) + k_l(z_0 - z_1)^2 + k_n(z_0 - z_1)^3$$

$$F_u(z_1, z_2) = k_u(z_1 - z_2),\ F_r(\dot{z}_1, \dot{z}_2) = k_r(\dot{z}_1 - \dot{z}_2)$$

and the nonlinear and linear stiffness of the suspension spring are k_n, k_l and k_m. The suspension damper coefficients are k_{c1} and k_{c2}. Correspondingly, k_u and k_r are the coefficients of equivalent spring and damper for wheel tire.

Benefiting from non-linear stiffness and passive damping properties, quasi-zero stiffness bioinspired dynamics resulted from an asymmetrical X-shape structure can effectively isolate vibrations while achieving excellent energy efficiency. Therefore, reference bioinspired dynamics with ideal damping are constructed elaborately in this article, as illustrated on the right-hand side of Fig. 2, to provide a reference trajectory for the plant. The implementation of the reference bioinspired dynamics is detailed in the next section.

B. Constrained Optimization

With the advent of emerging technologies, the acquisition of irregular road excitation information for autonomous vehicles has become possible. Feasible candidate solutions include detection via optical sensor or cloud-assisted network communication, as illustrated in Fig. 1. Inspired by the fact that human drivers slow down to reduce vibration when approaching a bump and accelerate to pass quickly when leaving it, an intuitive idea is to further optimize performance through velocity planning when global road information is assumed to be available. In detail, the optimization-based velocity planning problem can be formulated as striking a balance of the following aspects:

- Reasonable planned velocity (the vehicle acceleration constraint should be satisfied to avoid generating an unreasonable or unsatisfactory planned velocity).
- Vehicle body vibrations suppression (which can be quantified by the vertical acceleration of sprung mass).
- Fast passage of vehicle (which can be reflected intuitively by the vehicle passage time).
- Excellent longitudinal comfort (which can be evaluated by the vehicle longitudinal acceleration).

C. Performance Index

To quantity and compare effects of various control frameworks, the root mean square (RMS) of vehicle body acceleration [27] and positive mechanical power P^+ of actuator are introduced as performance indexes for ride comfort and energy consumption, respectively, as follow

$$RMS_{\ddot{z}_0} = \sqrt{\frac{1}{\mathcal{L}}\int_0^{\mathcal{L}} \ddot{z}_0^2 dt},\ RMS_{P^+} = \sqrt{\frac{1}{\mathcal{L}}\int_0^{\mathcal{L}} \left(P^+(t)\right)^2 dt} \tag{3}$$

where $\mathcal{L}$ denotes the time duration, and the power P^+ can be calculated as

$$P^+(t) = \begin{cases} u(t)(\dot{z}_0 - \dot{z}_1), & \text{for } u(t)(\dot{z}_0 - \dot{z}_1) > 0 \\ 0, & \text{else} \end{cases}$$

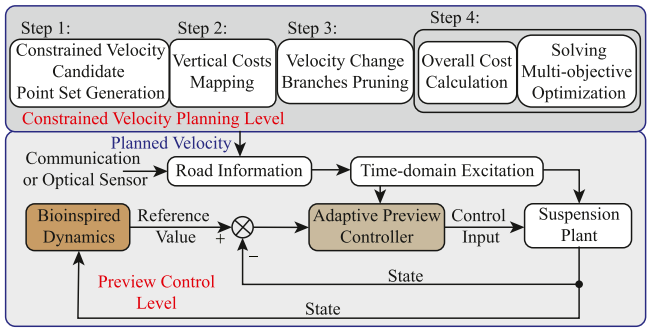

Fig. 3. Overview of the proposed method.

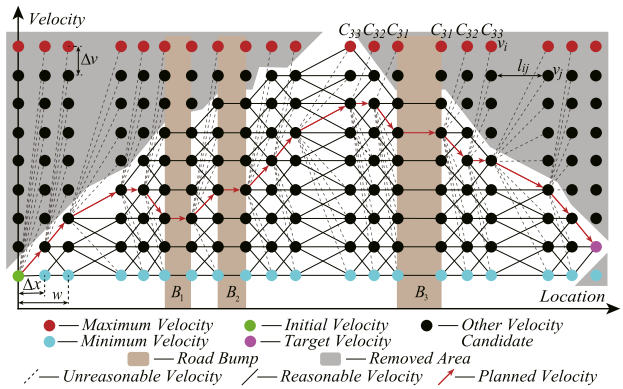

Fig. 4. Schematic of the constrained velocity planning.

III. Main Results

This section first provides details on how to optimize longitudinal and vertical performance simultaneously by searching for a reasonable velocity trajectory that satisfies constraints using road preview information as in Section III-A. Then, based on the planned velocity and corresponding road excitation, a preview adaptive suspension nonlinear controller that does not require optimization is designed in Section III-C by combining bionic dynamics, as in Section III-B, derived from the animal limb structure.

The schematic overview of the proposed method is illustrated in Fig. 3. Firstly, a constrained planned velocity trajectory can be obtained by solving a multi-objective optimization problem to balance the multi-dimensional performance cost. The corresponding time-domain road excitation can be generated employing the road information obtained from communication or optical sensors and the planned velocity. Then, the control input is calculated by means of the proposed adaptive preview controller.

A. Constrained Velocity Planning

Road preview information allows autonomous vehicles to adjust the planned velocity according to road conditions ahead in order to find the optimal trade-off between longitudinal and vertical performance, which is the primary issue in this subsection. First, as depicted in Fig. 4, the road ahead is partitioned depending on the locations of road bumps, with the both sides of bumps and the areas entering the end point or leaving the initial

point as speed regulation zones. Then, adjustment locations are selected with the spatial granularity Δx in adjustment areas. Each adjustment location contains a speed candidate set $S_v = \{v_{\min}, v_{\min} + \Delta v, \ldots, v_{\max}\}$, which is generated by velocity increment Δv from the minimum speed $v_{\min}$ to the maximum speed $v_{\max}$. The search space, as displayed in Fig. 4, consists of all velocity candidates of adjustment positions.

It is worth mentioning that a new efficient preview planning method is proposed in [14] by means of the speed candidate space above. Despite that, some key aspects still need to be improved: 1) The planned velocity is searched from the entire candidate space, which potentially results in unrealistic or unreasonable velocity changes between two adjacent velocity adjustment points. 2) One way to avoid this issue is to enlarge spatial granularity Δx, which means that a large regulation interval, namely, the speed regulation is not flexible enough. 3) An entire space search for all speed candidates would cause a high computational burden.

For this reason, an acceleration constrained planning algorithm is proposed and detailed in this subsection, where the assumptions remain the same as [14]. For clarity, an uneven road with three bumps is plotted as Fig. 4, where each speed regulation zone width is set to $w = 2\Delta x$.

Step 1: Velocity candidate points that do not satisfy the acceleration or deceleration limits are removed, as points contained in the removed areas in Fig. 4. That is, the corresponding velocity candidate is removed from the search space, if

$$\begin{cases} \frac{v_i^2 - v_{i+1}^2}{2l_{ij}} > d_{\max}, & \text{for } v_i \geq v_{i+1} \\ \frac{v_{i+1}^2 - v_i^2}{2l_{ij}} > a_{\max}, & \text{for } v_{i+1} > v_i \end{cases} \tag{4}$$

where positive constants $a_{\max}$ and $d_{\max}$ denote the preset maximum acceleration and deceleration, respectively. v_i and v_{i+1} denote two candidate velocities at adjacent positions and l_{ij} is the distance between them. One possible velocity search case is annotated in Fig. 4.

Step 2: Vertical costs of passing each adjustment location at feasible velocities are calculated to evaluate the vertical performance at various velocities. The vertical cost $C_i(B_i, v, \varpi_i)$ of passing i-th bump B_i of width ϖ_i with velocity $v \in S_v$ can be approximated as

$$C_i(B_i, v, \varpi_i) = \frac{v}{\varpi_i} \int_0^{\frac{\varpi_i}{v}} \left\{ \epsilon_1 \Upsilon_1^2(t) + \epsilon_2 \Upsilon_2^2(t) + \epsilon_3 \Upsilon_3^2(t) \right\} dt \tag{5}$$

where ϵ_1, ϵ_2 and ϵ_3 denote the weighting parameters of the corresponding vertical performance components $\Upsilon_1 = \ddot{z}_0$, $\Upsilon_2 = z_0 - z_1$, $\Upsilon_3 = z_1 - z_2$, respectively. Then, the vertical cost C_{ij} of the j -th column velocity candidate points in the left or right of i-th bump B_i can be expressed accordingly as

$$C_{ij}(B_i, v, \varpi_i) = \varrho^{j-1} C_i(B_i, v, \varpi_i), j = 1, \ldots, \frac{\varpi_i + \Delta x}{\Delta x} \tag{6}$$

where positive constant $\varrho \in (0, 1)$ is used to indicate that the vehicle is approaching or leaving a bump. As an illustration, for B_3 in Fig. 4, $C_{31} = C_3$, $C_{32} = \varrho C_3$, $C_{32} = \varrho^2 C_3$.

Step 3: Among the remaining velocity candidate points after *Step 1*, there are still velocity change branches that do not satisfy the constraints (4), which are removed in this step, and only reasonable velocity change branches are retained. For illustration purposes, one possible planned velocity is represented by red arrows in Fig. 4. The corresponding unreasonable velocity change branches, drawn as a dashed line, are deleted. Note that this operation is applied for all remaining velocity points when performing a velocity search maneuver, only a small portion is illustrated in Fig. 4 for clarity.

Step 4: With *Steps 1-3* described previously, a constrained multi-objective optimization problem that takes longitudinal and vertical performance into account is solved in this step to generate the optimal velocity trajectory. The overall cost function $\Xi(v_i, v_j)$ from velocity candidate v_i to next velocity candidate v_j in the adjacent position can be written as

$$\begin{aligned} \Xi(v_i, v_j) = \varkappa_1 \Gamma_1(v_i, v_j, l_{ij}) + \varkappa_2 \Gamma_2(v_i, v_j, l_{ij}) \\ + \varkappa_3 \Gamma_3(v_i, v_j, l_{ij}) \end{aligned} \tag{7}$$

where $\Gamma_1(v_i, v_j, l_{ij}) = C_{ij}(B_i, v, \varpi_i)$ represents the vertical ride comfort, $\Gamma_2(v_i, v_j, l_{ij}) = \left| \frac{v_i^2 - v_j^2}{2l_{ij}} \right|$ denotes the longitudinal acceleration is utilized to quantify longitudinal comfort, and $\Gamma_3(v_i, v_j, l_{ij}) = \left| \frac{2l_{ij}}{v_i + v_j} \right|$ is the vehicle passage time. $\varkappa_1$, $\varkappa_2$ and $\varkappa_3$ are the associated weights for the different performance indicators. Then the optimal desired velocity trajectory can be obtained, employing dynamic programming, by minimizing the following cost function

$$\Theta(v_m) = \min_{v_m, v_n \in S_v} \{ f(v_m, v_n) + \Theta(v_n) \} \tag{8}$$

where $f(v_m, v_n) = \Xi(v_m, v_n)$ if $v_m, v_n \in S_v$ are the velocity candidates in adjacent columns; Otherwise, $f(v_m, v_n) = \infty$.

The proposed constrained velocity planning algorithm has the following key features:

- Acceleration and deceleration limits (a_{max}, d_{max}) can be pre-specified arbitrarily and thus unreasonable velocity can be avoided.
- The spatial granularity Δx between adjacent locations and the width w of speed regulation zone can be set flexibly to meet user requirements.
- Compared to unconstrained velocity planning, the search space of the proposed algorithm and the corresponding computational burden are reduced by the considering constraints.
- Meanwhile, the optimality of the generated velocity trajectories is ensured.

The proposed constrained velocity planning is essentially an optimization problem, by minimizing overall cost consisting of the vehicle passage time Γ_3, the longitudinal comfort cost Γ_2, and the vertical ride comfort cost Γ_1, in the feasible velocity candidate set which satisfies the constraint (4). It can be concluded from (7) that the overall cost $\Xi(v_i, v_j)$ is a weighted sum of the vehicle passage time Γ_3, the longitudinal comfort cost Γ_2, and the vertical ride comfort cost Γ_1. As the weighting factor $\varkappa_i, i = 1, 2, 3$ of the corresponding cost indicator is larger, the proportion of the corresponding performance in the total weight

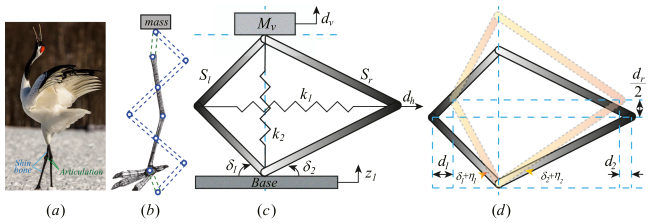

Fig. 5. Illustration of the limb-like bio-inspired dynamics. (a) A crane with its asymmetric bones and articulations. (b) Asymmetric X-shaped mechanisms exist in the leg. (c) Static bio-inspired structure. (d) Comparison after deformation, the deformed parts are shown in yellow.

increases, which implies a greater focus on the corresponding aspect. In practice, the weighting factors can be adjusted according to the actual requirements to balance the demand for various performances.

Remark 1: By design of the presented optimal constrained planning algorithm, spatial granularity Δx and velocity increment Δv can be set arbitrarily, while meeting acceleration limits. This ensures velocity feasibility and operation flexibility, which also helps to reduce the computational requirements by removing the unreasonable candidates.

Remark 2: Based on the planned longitudinal velocity trajectory and road information, the transformation approach in [14] can be used to generate time-domain road excitation. Note that the road information sampling time T is independent of the controller, which can be set arbitrarily to match the processing requirements. The time-domain excitation processing is detailed in [14].

B. Bioinspired Dynamics

Animal limb structures [28] with the notable capability to suppress vibration, such as the shin bones and articulation of a crane in Fig. 5(a), provide inspiration for vehicle suspension system. Exploiting beneficial nonlinearities by introducing the limb-inspired bionic structure contributes to achieving favorable performance at a lower cost. A common asymmetric structure, as displayed in Fig. 5(b), is modelled and introduced in this section to emulate this characteristic by exploiting beneficial nonlinearities. Noting that beneficial non-linearities present in the X-shaped mechanism are not only rigorously analyzed mathematically [29] but are deployed and validated on experimental platforms as in [28], [29]. By elaborately designing the X-shaped structure as in [29] and introducing it into the controller design to exploit the beneficial non-linearities can consequently achieve effective vibration isolation performance with less energy consumption. The geometric relationship of the asymmetric static bionic mechanism is drawn in Fig. 5(c). S_l and S_r denote the rods lengths on the left and right side with initial angle δ_1 and δ_2, respectively. k_1 and k_2 represent linear spring stiffness in horizontal and vertical directions. d_v is the vertical displacement of the sprung mass M, and road input or excitation is denoted as z_1.

To analyze the dynamic characteristics, the deformation comparisons are plotted in Fig. 5(d) where $\eta \triangleq \eta_1 + \eta_2$, $d_h \triangleq d_1 + d_2$ represent rotational and horizontal motion. The displacement of the sprung mass M_v relative to the base is defined as $d_r = d_v - z_1$. It is clear that

$$\eta_i = \arctan\left(\frac{S_i \sin\delta_i + \frac{d_r}{2}}{S_i \cos\delta_i - d_i}\right) - \delta_i \tag{9}$$

$$d_i = S_i \cos\delta_i - \sqrt{S_i^2 - \left(S_i \sin\delta_i + \frac{d_r}{2}\right)^2} \tag{10}$$

where $i = 1, 2$, $S_1 = S_l$, and $S_2 = S_r$.

With the aid of Hamilton principle, the bionic dynamics can be described as

$$M\ddot{d}_r + p_1(d_r) + k_2 d_r + \varsigma_1 \dot{d}_r + \varsigma_2 j_n p_2(d_r)\dot{d}_r = -M\ddot{z}_1 \tag{11}$$

where ς_1, ς_2 indicate the air drag and friction factor. And $p_1(d_r) = k_1 d_h \frac{d(d_h)}{d(d_r)} \frac{d(d_r)}{d(d_v)}$, $p_2(d_r) = \left(\frac{d\eta}{d(d_r)}\right)^2$ can be further determined by combining geometric relationship (9), (10) mentioned above, as

$$\begin{aligned} p_1(d_r) = \frac{k_1}{2}\Bigg(& S_l\cos\delta_1 + S_r\cos\delta_2 - \sqrt{S_l^2 - \xi^2(d_r)} \\ & - \sqrt{S_r^2 - \xi^2(d_r)}\Bigg) \\ & \times \left(\frac{\xi(d_r)}{\sqrt{S_l^2 - \xi^2(d_r)}} + \frac{\xi(d_r)}{\sqrt{S_r^2 - \xi^2(d_r)}}\right) \end{aligned}$$

$$p_2(d_r) = \left(\frac{1}{2\sqrt{S_l^2 - \xi^2(d_r)}} + \frac{1}{2\sqrt{S_r^2 - \xi^2(d_r)}}\right)^2$$

where $\xi(d_r) \triangleq S_l \sin\delta_1 + \frac{d_r}{2}$.

When the bioinspired dynamics are applied to autonomous vehicles, the structure and parameters can be chosen rationally according to the bionic dynamic properties as in [29], while the unsprung acceleration signal $\ddot{z}_1$ is obtained by the sensor, then the reference is achievable.

Remark 3: The road excitation information $z_2, \dot{z}_2$ can be incorporated into the adaptive control framework by taking $z_0 - z_1$ and $\dot{z}_0 - \dot{z}_1$ as the state variables. However, this poses an additional problem: how to determine the corresponding reference trajectory. 0 is taken as the reference in the most existing results, which is unreasonable obviously, for example a continuous sinusoidal pavement. The sinusoidal reference is also used, which is still doubtful, e.g. a flat road. The bionic dynamics in this section provides a viable reference that isolates vibration while reducing energy consumption.

Remark 4: The introduced bionic dynamics contribute to reducing energy consumption by employing beneficial nonlinearities. Nonetheless, the bionic model constructed in this article is more suitable for urban road scenarios. The performance of the bionic dynamics is closely related to the bionic structure and its parameters, such as the asymmetric rod length. When excessively severe road excitation occurs, the direct introduction of the bionic structure designed in this article may not achieve

desired results. For special road scenarios, such as off-road terrain and mountainous regions, further adjustments are required depending on the road excitation and bionic dynamics response characteristics [29].

C. Adaptive Preview Control Design

Let vehicle suspension deflection $s_d \triangleq z_0 - z_1$ and its dynamic $r_d \triangleq \dot{z}_0 - \dot{z}_1$ be the state variables, in the light of (1) and (2), the suspension model can be rearranged as

$$\dot{s}_d = r_d \tag{12}$$

$$\dot{r}_d = \Lambda^T \psi + \frac{1}{\gamma} u + \mathcal{Z} + \mathcal{R} \tag{13}$$

where $\Lambda \triangleq [-\frac{k_m}{m_0}, -\frac{k_l}{m_0}, -\frac{k_n}{m_0}, -\frac{k_{c1}}{m_0}, -\frac{k_{c2}}{m_0}]^T$ and $\gamma \triangleq \frac{m_0 m_1}{m_0+m_1}$ are unknown because it contains uncertain sprung mass $m_0 \in (m_{\min}, m_{\max})$, and thus, $\gamma \in (\frac{m_{\min} m_1}{m_{\min}+m_1}, \frac{m_{\max} m_1}{m_{\max}+m_1})$. $\psi \triangleq [s_d, s_d^2, s_d^3, r_d, r_d^2]^T$ and $\mathcal{Z} \triangleq -\frac{k_m}{m_1}(z_0 - z_1) - \frac{k_l}{m_1}(z_0 - z_1)^2 - \frac{k_n}{m_1}(z_0 - z_1)^3 - \frac{k_{c1}}{m_1}(\dot{z}_0 - \dot{z}_1) - \frac{k_{c2}}{m_1}(\dot{z}_0 - \dot{z}_1)^2 + \frac{k_u}{m_1} z_1 + \frac{k_r}{m_1}\dot{z}_1$ are known vector. $\mathcal{R} = -\frac{k_u}{m_1} z_2 - \frac{k_r}{m_1}\dot{z}_2$ denotes the road excitation information, which can be obtained by the optical sensor or wireless network communication. Subsequently, an adaptive controller is synthesized to track the desired bioinspired dynamics (11).

Step 1: Develop virtual controller α_1 in this step so that s_d is capable of tracking the reference trajectory s_{dr}.

The tracking errors are defined as

$$e_1 = s_d - s_{dr}, e_2 = r_d - r_{dr} - \alpha_1 \tag{14}$$

where s_{dr} and r_{dr} are the reference trajectory for s_d, r_d which can be calculated from bioinspired dynamics (11). α_1 denotes the virtual control input, based on (12)–(14), we have

$$\dot{e}_1 = e_2 + \alpha_1 \tag{15}$$

Aiming to track the desired trajectory s_{dr} generated from the bionic dynamics (11), the virtual control input α_1 is designed as

$$\alpha_1 = -\rho_1 e_1 \tag{16}$$

where the parameter $\rho_1 \in \mathbb{R}^+$ is manually set to achieve satisfactory performance. Obviously, with the virtual control input (16), the differential inequality $\dot{V}_1 \leq 0$ of Lyapunov function $V_1 = \frac{1}{2}\rho_1 e_1^2$ holds when $e_2 = 0$. This means that s_{dr} can be tracked asymptotically, if $e_2 = 0$, with the virtual controller (16). To ensure e_2 can converge to 0, design controller u in *Step 2*.

Step 2: To further ensure that the asymptotic convergence of tracking error e_2 with uncertain parameter m_0 is achieved, the controller u and adaptive laws are given in this step.

Combining (15) with (16), we get

$$e_1 \dot{e}_1 = -\rho_1 e_1^2 + e_1 e_2 \tag{17}$$

Invoking (13) and bionic dynamic (11), the error dynamic of e_2 can be expressed as

$$\dot{e}_2 = \Lambda^T \psi + \frac{1}{\gamma} u + \mathcal{Z} + \mathcal{R} - \dot{r}_{dr} - \dot{\alpha}_1 \tag{18}$$

The estimations of uncertain vector Λ and γ are denoted as $\hat{\Lambda}$ and $\hat{\gamma}$. Correspondingly, the resulting estimate errors are written as $\tilde{\gamma} \triangleq \hat{\gamma} - \gamma$ and $\tilde{\Lambda} \triangleq \hat{\Lambda} - \Lambda$. Finally, the controller u is given by

$$u = \hat{\gamma}(-\rho_2 e_2 - e_1 - \hat{\Lambda}^T \psi - \mathcal{Z} - \mathcal{R} + \dot{r}_{dr} + \dot{\alpha}_1) \tag{19}$$

where $\rho_2 \in \mathbb{R}^+$ and the rate of convergence of e_2 can be adjusted by adapting parameter ρ_2. Meanwhile, the adaptive laws are developed as

$$\dot{\hat{\Lambda}} = \mathcal{K}^{-1} e_2 \psi, \ \dot{\hat{\gamma}} = \ \text{Proj}_\gamma \tag{20}$$

where $\mathcal{K} = \text{diag}(\kappa_1, \kappa_2, \kappa_3)$ is an invertible diagonal matrix with the design parameters $\kappa_i, i = 1, 2, 3$. The projection operation Proj_γ can be stated as

$$\text{Proj}_\gamma = \begin{cases} 0, & \text{if } \hat{\gamma} = \frac{m_{\max} m_1}{m_{\max}+m_1} \text{ and } \dot{\hat{\gamma}}_0 > 0 \\ 0, & \text{if } \hat{\gamma} = \frac{m_{\min} m_1}{m_{\min}+m_1} \text{ and } \dot{\hat{\gamma}}_0 < 0 \\ \dot{\hat{\gamma}}_0, & \text{otherwise.} \end{cases}$$

with $\dot{\hat{\gamma}}_0 = \vartheta e_2(\rho_2 e_2 + e_1 + \hat{\Lambda}^T \psi + \mathcal{Z} + \mathcal{R} - \dot{r}_{dr} - \dot{\alpha}_1)$, $\vartheta \in \mathbb{R}^+$.

By design of the virtual control input (16), the controller (19), and the adaptive laws (20), the reference bionic dynamics tracking errors e_1, e_2 converge asymptotically to the origin.

The asymptotic convergence is proved with the following Lyapunov function candidate

$$V = \frac{1}{2} e_1^2 + \frac{1}{2} e_2^2 + \frac{1}{2\vartheta\gamma}\tilde{\gamma}^2 + \frac{1}{2}\tilde{\Lambda}^T \mathcal{K} \tilde{\Lambda} \tag{21}$$

The derivative of (21) with respect to time can be represented as

$$\dot{V} = e_1 \dot{e}_1 + e_2 \dot{e}_2 + \frac{1}{\vartheta\gamma}\tilde{\gamma}\dot{\tilde{\gamma}} + \tilde{\Lambda}^T \mathcal{K} \dot{\tilde{\Lambda}}$$

Combining (18) and the designed controller (19) yields

$$\begin{aligned} \dot{V} = & -\rho_1 e_1^2 + e_2 \left(e_1 + \Lambda^T \psi + \frac{1}{\gamma} u + \mathcal{Z} + \mathcal{R} - \dot{r}_{dr} - \dot{\alpha}_1 \right) \\ & + \frac{1}{\vartheta\gamma}\tilde{\gamma}\dot{\tilde{\gamma}} + \tilde{\Lambda}^T \mathcal{K} \dot{\tilde{\Lambda}} \\ = & -\rho_1 e_1^2 - \rho_2 e_2^2 + \frac{1}{\vartheta\gamma}\tilde{\gamma} e_2 \vartheta(-\rho_2 e_2 - e_1 - \hat{\Lambda}^T \psi - \mathcal{Z} \\ & - \mathcal{R} + \dot{r}_{dr} + \dot{\alpha}_1) + \frac{1}{\vartheta\gamma}\tilde{\gamma}\dot{\tilde{\gamma}} + \tilde{\Lambda}^T \mathcal{K} \dot{\tilde{\Lambda}} - e_2 \tilde{\Lambda}^T \psi \end{aligned}$$

By invoking the adaptive laws (20), we obtain

$$\begin{aligned} \dot{V} = & -\rho_1 e_1^2 - \rho_2 e_2^2 + \frac{1}{\vartheta\gamma}\tilde{\gamma} e_2 \vartheta(-\rho_2 e_2 - e_1 - \hat{\Lambda}^T \psi \\ & - \mathcal{Z} - \mathcal{R} + \dot{r}_{dr} + \dot{\alpha}_1) + \frac{1}{\vartheta\gamma}\tilde{\gamma}\text{Proj}_\gamma \\ & + \tilde{\Lambda}^T \mathcal{K} \mathcal{K}^{-1} e_2 \psi - e_2 \tilde{\Lambda}^T \psi \\ \leq & -\rho_1 e_1^2 - \rho_2 e_2^2 \leq 0 \end{aligned}$$

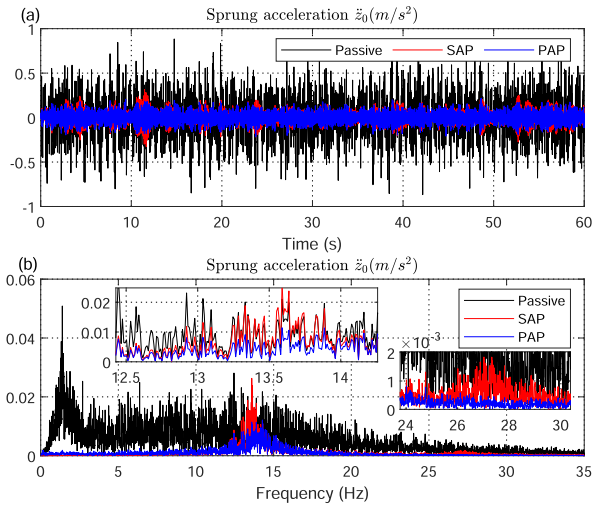

Fig. 6. Sprung mass acceleration $\ddot{z}_0$. (a) Time-domain response of $\ddot{z}_0$. (b) Frequency component of $\ddot{z}_0$ by fast fourier transform.

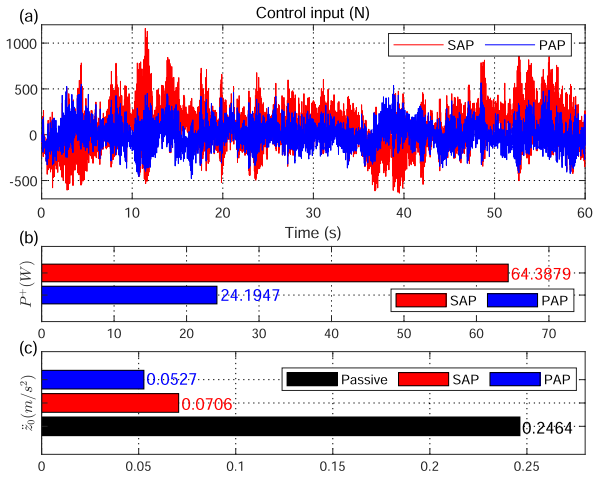

Fig. 7. Control input and quantitative comparison. (a) Control input. (b) RMS of the actuator power P^+. (c) RMS of the acceleration $\ddot{z}_0$.

Following the stability analysis in [18], [21], we can obtain $\dot{V} \to 0$ when $t \to \infty$ by employing LaSalle invariance principle, correspondingly, e_1 and e_2 converge to 0 asymptotically.

Remark 5: Classic adaptive control methods take the displacement z_0 and velocity $\dot{z}_0$ of the sprung mass m_0 as state variables [18], namely, $x_1 = z_0, x_2 = \dot{z}_0$. The controller $u(t)$ is developed based on the dynamics equations of m_0 as follows

$$\dot{x}_1 = x_2 \tag{22}$$

$$m_0 \dot{x}_2 = -F_k(z_0, z_1) - F_c(\dot{z}_0, \dot{z}_1) + u(t) \tag{23}$$

Clearly, (23) do not contain the road excitation which is isolated by the unsprung mass m_1. This means that it cannot be applied for preview suspension control.

Remark 6: To the best of the authors' knowledge, the proposed nonlinear adaptive preview controller has a simple structure with low computational requirements, which does not rely on a simplified linear model or optimization, and is proposed for the first time in this article. Meanwhile, unlike conventional nonlinear adaptive controllers [27] based on the unsprung subsystem that cannot be applied to preview suspension, the presented controller provides a novel way to handle nonlinear preview suspension control.

IV. Comparative Study

A. Preview Controller Performance

Based on the Hyundai Elantra suspension, the effectiveness of the proposed adaptive preview control method is tested and analyzed by means of a B-class random road obtained via the filtered white noise method. The bionic dynamics provides a reference trajectory for the preview suspension, where the suspension (1)–(2) parameters: $m_0 = 240$ kg, $m_1 = 23.61$ kg, $k_m = 15394$ N/m, $k_l = -73696$ N/m^2, $k_n = 3170400$ N/m^3, $k_{c1} = 1385.4$ Ns/m, $k_{c2} = 524.28$ Ns/m^2, $k_u = 181818.88$ N/m, $k_r = 138$ Ns/m. And 12.5% sprung mass uncertainty is assumed, namely, $m_{\min} = 0.875m_0$, $m_{\max} = 1.125m_0$. The uncertain parameter sprung mass m_0 is initially chosen as $m_{\min}$, correspondingly, $\Lambda(0) \triangleq [-\frac{k_m}{m_{\min}}, -\frac{k_l}{m_{\min}}, -\frac{k_n}{m_{\min}}, -\frac{k_{c1}}{m_{\min}}, -\frac{k_{c2}}{m_{\min}}]^T$ and $\gamma(0) \triangleq \frac{m_{\min} m_1}{m_{\min}+m_1}$. The settings of bioinspired reference model (11) are chosen as: $M_v = 960$ kg, $\delta_1 = \frac{\pi}{6}$ rad, $S_l = 0.1$ m, $S_r = 0.2$ m, $\varsigma_1 = 50$ Ns/m, $\varsigma_2 = 0.15$ Ns/m, $k_2 = 350$ N/m, $k_1 = 500$ N/m.

In order to analyze and evaluate control effectiveness, the suspension performances in the following cases are provided.

- Passive: Passive suspension.
- SAP: A classical standard adaptive control method which is designed based on the suspension sprung mass dynamics (22)–(23), as stated in *Remark 5*. The controller structure is detailed in [18], [21] with parameters settings $k_1 = 1 \times 10^4, k_2 = 20$ in the comparative results. The reference values of the sprung mass states z_0 and $\dot{z}_0$ are set to 0.
- PAP: The proposed preview adaptive controller is given in (19) with $\rho_1 = 1 \times 10^4$, $\rho_2 = 20$, $\kappa_1 = \kappa_2 = \kappa_3 = 1$, $\vartheta = 1$. And the reference trajectories s_{dr}, r_{dr} are obtained by the bioinspired dynamics (11).

Sprung mass acceleration $\ddot{z}_0$ comparative results are illustrated in Fig. 6 to evaluate the vehicle ride comfort where the vehicle velocity is chosen as 36 km/h. As shown in Fig. 6(a), the active suspension controller SAP enables effective vibration isolation caused by uneven road excitation. Moreover, the vertical vibration is further suppressed by the PAP employing road preview information, which means that the ride comfort performance is further enhanced. In particular, the high-frequency vibrations are significantly reduced as seen in Fig. 6(b).

The control inputs of SAP and the proposed PAP are reported in Fig. 7(a). Benefiting from the bionic dynamics, PAP can achieve better ride comfort with fewer control input requirements than SAP by exploiting beneficial non-linearities, which contribute to reducing energy consumption. RMS_{P^+} and $RMS_{\ddot{z}_0}$ as performance indexes of energy consumption and ride comfort defined in (3) are calculated and plotted in Fig. 7(b) and (c) for quantitative evaluation. Compared with SAP, the RMS_{P^+} of PAP is significantly reduced (over 60%) while

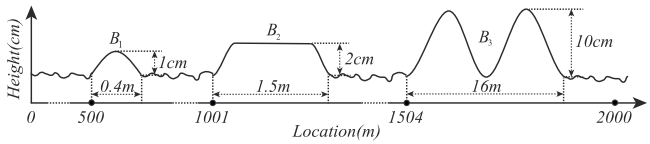

Fig. 8. Uneven road.

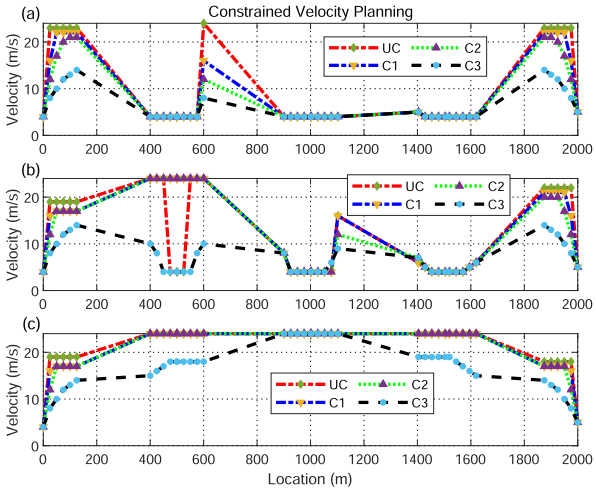

Fig. 9. Planned velocity trajectories subject to different constraints.

$RMS_{\ddot{z}_0}$ is also reduced (over 25%). This means that effective energy saving is achieved and ride comfort is further improved by the presented PAP.

B. Preview Control With Constrained Velocity Planning

Comparative results are provided in this subsection to prove the advantages and effectiveness of the constrained velocity planning method detailed above, based on the uneven road (UR) comprising bumps (B_1, B_2, B_3) and random roads. As depicted in Fig. 8, the typical uneven road conditions, such as speed bumps, manhole covers, and slopes, are modeled by choosing different bumps settings.

As described in Fig. 4, the initial velocity and target velocity in start location 0 m and end location 2000 m are set to 4 m/s and 5 m/s in this study. The maximum velocity $v_{\max}$ and minimum velocity $v_{\min}$ are 4 m/s and 24 m/s. The vertical costs $C_i(B_i, v, \varpi_i), i = 1, 2, 3$ are approximated with $\epsilon_1 = 20$, $\epsilon_2 = 1$, $\epsilon_3 = 1$, and $\varrho = 0.5$ in *Step 2* . Meanwhile, to generate the velocity candidate set in each adjustment location for bumps, initial point, and target point, the velocity increment Δv, spatial granularity Δx, and speed regulation zone width w are chosen as 1 m/s, 25 m, and 100 m, respectively.

The results in the following cases are presented in Fig. 9 to analyze the effects of the acceleration constraints: *UC* (unconstrained velocity planning), *C1* ($a_{\max} = 5$ m/s^2, $d_{\max} = -5$ m/s^2), *C2* ($a_{\max} = 3$ m/s^2, $d_{\max} = -3$ m/s^2), *C3* ($a_{\max} = 1$ m/s^2, $d_{\max} = -1$ m/s^2). The planned velocity trajectories generated by selecting cost weight parameters $\varkappa_1 = 10$, $\varkappa_2 = 1$, $\varkappa_3 = 1$ are shown in Fig. 9(a). It can be observed that the *UC* generates unrealistic velocity changes to reduce Γ_3 and Γ_1 when leaving B_1 and entering B_2. The changes in speed result in

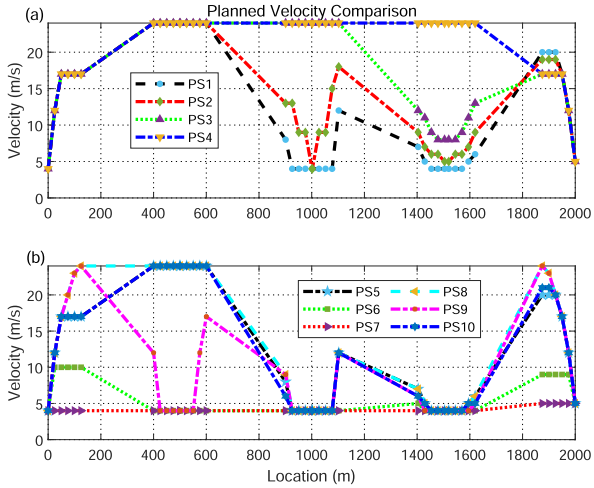

Fig. 10. Planned velocity trajectories subject to $C2$ generated with various weighting parameter settings.

acceleration and deceleration that exceed the desired constraints. The parameters are chosen as $\varkappa_1 = 10$, $\varkappa_2 = 10$, $\varkappa_3 = 10$ to strike a balance, as depicted in Fig. 9(b). Using the *UC* method, the vehicle enters B_1 with a sharp deceleration to suppress vibration and leaves B_1 with a high acceleration to reduce Γ_3. The unreasonable speed changes are avoided effectively when constraints are considered. However, the *UC* is particularly susceptible to violating the constraints. With the parameter settings (*PS*) $\varkappa_1 = 0.01$, $\varkappa_2 = 10$, $\varkappa_3 = 10$ as in Fig. 9(c), the planned velocities obtained by *C1*, *C2*, *C3* increase to $v_{\max}$ rapidly while satisfying the constraints. Note that this allows to set the spatial granularity Δx arbitrarily through the proposed constrained velocity planning, as the constraints satisfaction means that the unreasonable velocity changes at a small Δx are avoided.

An additional advantage of the proposed constrained velocity planning is that the search space is refined as elaborated in Fig. 4. The velocity candidate points and branches that do not satisfy the constraints are removed, which contributes to reduce the computational demand. Each planning algorithm is executed 50 times with computer configurations in [30] and the average execution times of for *UC*, *C1*, *C2*, and *C3* are 22.4 ms 22 ms, 21.4 ms, and 17.9 ms. In contrast to *UC*, the solution times of *C1*, *C2*, and *C3* are reduced by more than 2%, 4%, and 19%, respectively.

The comparative planned trajectories illustrated in Fig. 10 are used to analyze the role of the each cost weighting parameter. From the planned trajectories with *PS1* ($\varkappa_1 = 10$, $\varkappa_2 = 10$, $\varkappa_3 = 10$), *PS2* ($\varkappa_1 = 1$, $\varkappa_2 = 10$, $\varkappa_3 = 10$), *PS3* ($\varkappa_1 = 0.1$, $\varkappa_2 = 10$, $\varkappa_3 = 10$) and *PS4* ($\varkappa_1 = 0.01$, $\varkappa_2 = 10$, $\varkappa_3 = 10$) in Fig. 10(a), it can be seen that the vehicle tends to a higher speed as the vertical cost weighting parameter $\varkappa_1$ decreases. As displayed in Fig. 10(b) with *PS5* ($\varkappa_1 = 0.1$, $\varkappa_2 = 0.1$, $\varkappa_3 = 0.1$), *PS6* ($\varkappa_1 = 0.1$, $\varkappa_2 = 0.1$, $\varkappa_3 = 0.01$), and *PS7* ($\varkappa_1 = 0.1$, $\varkappa_2 = 0.1$, $\varkappa_3 = 0.001$), when $\varkappa_3$ decreases, the vehicle attempts to maintain a low speed and avoid speed variation. The smaller parameter $\varkappa_3$ means that the increased importance of ride comfort and longitudinal performance. In particular, as can be seen from *PS7*, the vehicle maintains the minimum

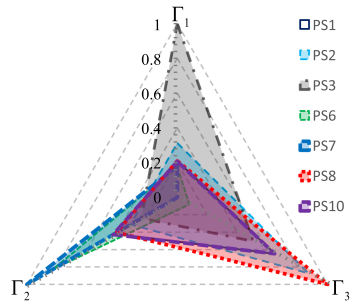

Fig. 11. Multiple objectives optimization.

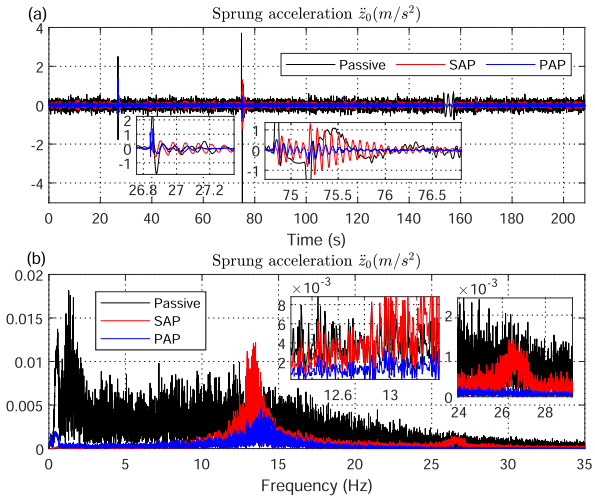

Fig. 12. Sprung mass acceleration $\ddot{z}_0$ for UR with constrained velocity planning. (a) Time-domain response of $\ddot{z}_0$ for UR. (b) Frequency component of $\ddot{z}_0$ for UR.

velocity and accelerates at the final stage to reach the target velocity. Compared to the *PS5*, the vehicle with *PS8* ($\varkappa_1 = 0.1$, $\varkappa_2 = 0.01$, $\varkappa_3 = 0.1$) tends to accelerate and decelerate rapidly to reduce vibration and Γ_3. Possible trajectories that consider Γ_1, Γ_2 and Γ_3 simultaneously are plotted as *PS9* ($\varkappa_1 = 10$, $\varkappa_2 = 2$, $\varkappa_3 = 6$) and *PS10* ($\varkappa_1 = 15$, $\varkappa_2 = 10$, $\varkappa_3 = 11$). *PS9* puts more emphasis on ride comfort, and *PS10* is more balanced.

Further, to reflect the performance trade-offs, the cost distribution of representative velocity trajectories is shown in Fig. 11. For clarity, the costs are normalized, with 1 denoting the maximum cost of each performance index in all selected trajectories. The remaining costs are transformed as the proportion relative to the maximum cost. Combined with Fig. 10, the planned velocity generation depends on the relative size of the weighting parameters, and the larger weighting parameters indicates more emphasis on that aspect. Considering the multi-objective performance, the velocity with *PS10* is chosen as the final planned trajectory. Then, the spatial road excitation is converted into temporal excitation using transformation method in [14] with the aid of the final velocity trajectory. Comparative simulations are carried out based on the passive, SAP, and PAP with the same controller parameters mentioned above.

As observed in Fig. 12(a), vehicle vibrations caused by uneven roads can be effectively isolated by the SAP and PAP. Making use of the preview road information, the PAP further improves ride

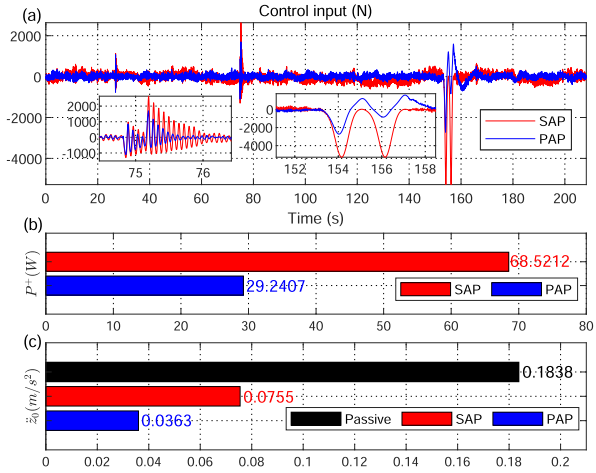

Fig. 13. Quantitative comparison for UR with constrained velocity planning. (a) Control input for UR. (b) RMS of the actuator power P^+ for UR. (c) RMS of the acceleration $\ddot{z}_0$ for UR.

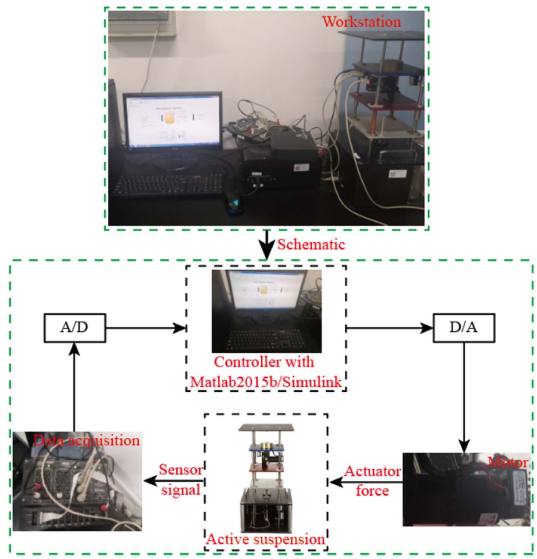

Fig. 14. Suspension experimental setup. D/A and A/D denote Digital-to-Analog conversion and Analog-to-Digital conversion, respectively.

comfort. Another major advantage the PAP can offer is the small computational burden. With the above controller parameters and the computer configurations in [30], the execution time of PAP is about 11.9 s. The adaptive control method demands low computational resources because no optimization is required. Moreover, the benefit and enhancement in terms of ride comfort achieved by PAP are further illustrated through the frequency components of $\ddot{z}_0$ displayed in Fig. 13(b).

In addition, from Fig. 13(a), PAP requires less control amplitude to suppress vibration. An interesting phenomenon observed in Fig. 13(a) is that the control input of SAP is distinct from PAP. A key reason for this is that the reference values for SAP are set to 0, whereas the reference trajectory for PAP is provided by the elaborately designed bionic dynamics (11). The RMS of P^+ and $\ddot{z}_0$ are calculated quantitatively and given in Fig. 13(b) and (c). The energy consumption of the PAP is reduced by more than

TABLE I
BIONIC DYNAMICS PARAMETERS

Term	Value	Term	Value	Term	Value
M_v	3 kg	δ_1	$\frac{\pi}{6}$ rad	S_l	0.1 m
S_r	0.2 m	ς_1	5 Ns/m	ς_2	0.15 Ns/m
k_1	500 N/m	k_2	350 N/m		

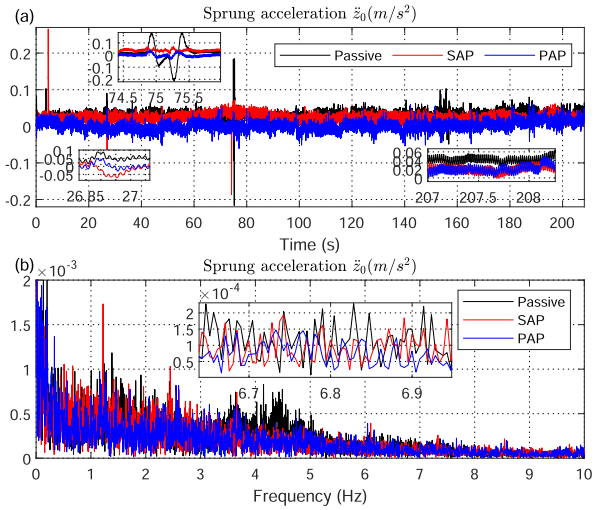

Fig. 15. Sprung mass acceleration $\ddot{z}_0$ obtained by experiment. (a) Time-domain response of $\ddot{z}_0$. (b) Frequency component of $\ddot{z}_0$.

57% compared to the SAP. Also, the $RMS_{\ddot{z}_0}$ is reduced by more than 51%.

C. Experiment Results

The proposed method is experimentally validated using the platform as in Fig. 14. The real-time motion information of the active suspension is obtained through sensors and data acquisition devices. The road excitation z_2 generated in the previous subsection employing the presented constrained velocity planning is reduced to $\frac{1}{10}z_2$ as the road input for this subsection. To avoid exceeding the limitations of the experimental setup, the height of B_3 is reduced to 3 cm. The suspension parameters can be obtained from [31]. The SAP controller parameters are set as $k_1 = 80, k_2 = 20$ with PAP parameters $\rho_1 = 100$, $\rho_2 = 20$, $\kappa_1 = \kappa_2 = \kappa_3 = 1$, $\vartheta = 1$. The bionic dynamics parameters setting is shown in Table I.

The time-domain response of $\ddot{z}_0$ experimentally obtained in Fig. 15(a) show that the vibration is suppressed, especially at the bumps. Meanwhile, from the frequency components in Fig. 15(b), it can be seen that the ride comforts of both SAP and PAP are enhanced compared to the passive suspension. Moreover, the sprung acceleration $\ddot{z}_0$ is further reduced by considering the road preview information in the controller design.

Fig. 16(c) illustrates quantitatively the advantage of the adaptive preview suspension control algorithm in terms of ride comfort. Compared to passive suspension, the RMS of $\ddot{z}_0$ is reduced by over 18% and 48% for SAP and PAP, respectively. Note that control inputs of PAP in Fig. 16(a) are generated from a bionic perspective, which differ significantly from SAP because of the bio-inspired dynamics. The PAP reduces the RMS of $\ddot{z}_0$ by about

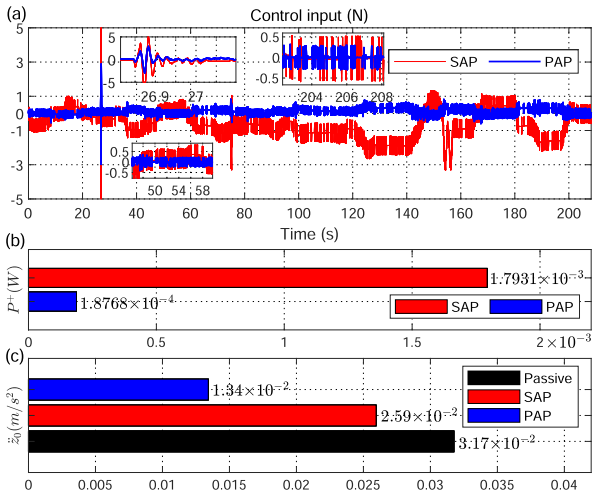

Fig. 16. Control input and quantitative comparison obtained by experiment. (a) Control input. (b) RMS of P^+. (c) RMS of $\ddot{z}_0$.

48% in comparison with SAP, while the RMS of P^+ is reduced by about 89% by introducing bionic dynamics as in Fig. 16(b).

V. CONCLUSION

This article presents a novel adaptive preview suspension control method that is not dependent on a simplified linear state space model and does not require optimization for the first time. Meanwhile, drawing inspiration from the animal limb structure, bioinspired dynamics are used to provide reference trajectories. Accordingly, the controller has a simple structure, low computational burden, and energy efficiency. Employing road preview information, a constrained velocity planning approach is proposed to balance vertical ride comfort, vehicle passage time, and longitudinal comfort. Not only is the restriction on the spatial granularity Δx eliminated, but unreasonable velocity changes are avoided. Comparative simulations and experiments demonstrate the effectiveness and advantages of the whole framework including constrained velocity planning and adaptive preview controller.

Future work focuses on introducing path planning to bypass some severe road bulges or depressions by using preview road information in the proposed velocity planning and preview control framework to further balance multi-objective costs and improve ride comfort. Meanwhile, at the control level, actuator failures, dead zones, time delays, and hysteresis can be further considered. Faster finite time and fixed time convergence are expected, while transient performance and state constraints can be satisfied by employing invertible transformations or barrier functions.

REFERENCES

[1] H. Taghavifar and S. Rakheja, "Multi-objective optimal robust seat suspension control of off-road vehicles in the presence of disturbance and parametric uncertainty using metaheuristics," *IEEE Trans. Intell. Veh.*, vol. 5, no. 3, pp. 372–384, Sep. 2020.

[2] J. J. Rath, M. Defoort, C. Sentouh, H. R. Karimi, and K. C. Veluvolu, "Output-constrained robust sliding mode based nonlinear active suspension control," *IEEE Trans. Ind. Electron.*, vol. 67, no. 12, pp. 10652–10662, Dec. 2020.
[3] H. Li, X. Jing, H.-K. Lam, and P. Shi, "Fuzzy sampled-data control for uncertain vehicle suspension systems," *IEEE Trans. Cybern.*, vol. 44, no. 7, pp. 1111–1126, Jul. 2014.
[4] H. Pan, X. Chang, and W. Sun, "Multitask knowledge distillation guides end-to-end lane detection," *IEEE Trans. Ind. Inform.*, vol. 19, no. 9, pp. 9703–9712, Sep. 2023.
[5] L. Chen et al., "Milestones in autonomous driving and intelligent vehicles: Survey of surveys," *IEEE Trans. Intell. Veh.*, vol. 8, no. 2, pp. 1046–1056, Feb. 2023.
[6] T. Huang, J. Wang, H. Pan, and W. Sun, "Finite-time fault-tolerant integrated motion control for autonomous vehicles with prescribed performance," *IEEE Trans. Transport. Electrific.*, early access, Dec. 26, 2022, doi: 10.1109/TTE.2022.3232521.
[7] X. Wang and W. Sun, "Trajectory tracking of autonomous vehicle: A differential flatness approach with disturbance-observer-based control," *IEEE Trans. Intell. Veh.*, vol. 8, no. 2, pp. 1368–1379, Feb. 2023.
[8] H. Pan, Y. Hong, W. Sun, and Y. Jia, "Deep dual-resolution networks for real-time and accurate semantic segmentation of traffic scenes," *IEEE Trans. Intell. Transp. Syst.*, vol. 24, no. 3, pp. 3448–3460, Mar. 2023.
[9] F.-Y. Wang, "Parallel control and management for intelligent transportation systems: Concepts, architectures, and applications," *IEEE Trans. Intell. Transp. Syst.*, vol. 11, no. 3, pp. 630–638, Sep. 2010.
[10] D. Cao et al., "Future directions of intelligent vehicles: Potentials, possibilities, and perspectives," *IEEE Trans. Intell. Veh.*, vol. 7, no. 1, pp. 7–10, Mar. 2022.
[11] M. Rahman and G. Rideout, "Using the lead vehicle as preview sensor in convoy vehicle active suspension control," *Veh. Syst. Dyn.*, vol. 50, no. 12, pp. 1923–1948, 2012.
[12] A. Akbari and B. Lohmann, "Output feedback H∞/GH2 preview control of active vehicle suspensions: A comparison study of LQG preview," *Veh. Syst. Dyn.*, vol. 48, no. 12, pp. 1475–1494, 2010.
[13] M. D. Donahue and J. K. Hedrick, "Implementation of an active suspension, preview controller for improved ride comfort," M.S. thesis, Master of Sci. (Plan II). Boston Univ., Univ. of California at Berkeley, Berkeley, CA, USA, 2001.
[14] J. Wu, H. Zhou, Z. Liu, and M. Gu, "Ride comfort optimization via speed planning and preview semi-active suspension control for autonomous vehicles on uneven roads," *IEEE Trans. Veh. Technol.*, vol. 69, no. 8, pp. 8343–8355, Aug. 2020.
[15] C. Gohrle, A. Schindler, A. Wagner, and O. Sawodny, "Design and vehicle implementation of preview active suspension controllers," *IEEE Trans. Control Syst. Technol.*, vol. 22, no. 3, pp. 1135–1142, May 2014.
[16] J. Theunissen et al., "Regionless explicit model predictive control of active suspension systems with preview," *IEEE Trans. Ind. Electron.*, vol. 67, no. 6, pp. 4877–4888, Jun. 2020.
[17] A. Soliman and D. Crolla, "Limited bandwidth active suspension employing wheel base preview," SAE Tech. Paper, Tech. Rep. 2001-01-1063, 2001.
[18] W. Sun, H. Gao, and O. Kaynak, "Adaptive backstepping control for active suspension systems with hard constraints," *IEEE/ASME Trans. Mechatron.*, vol. 18, no. 3, pp. 1072–1079, Jun. 2013.
[19] H. Pan, X. Jing, W. Sun, and Z. Li, "Analysis and design of a bioinspired vibration sensor system in noisy environment," *IEEE/ASME Trans. Mechatron.*, vol. 23, no. 2, pp. 845–855, Apr. 2018.
[20] X. Jing, Y. Chai, X. Chao, and J. Bian, "In-situ adjustable nonlinear passive stiffness using X-shaped mechanisms," *Mech. Syst. Signal Process.*, vol. 170, 2022, Art. no. 108267.
[21] H. Pan, X. Jing, W. Sun, and H. Gao, "A bioinspired dynamics-based adaptive tracking control for nonlinear suspension systems," *IEEE Trans. Control Syst. Technol.*, vol. 26, no. 3, pp. 903–914, May 2018.
[22] F.-Y. Wang et al., "Verification and validation of intelligent vehicles: Objectives and efforts from China," *IEEE Trans. Intell. Veh.*, vol. 7, no. 2, pp. 164–169, Jun. 2022.
[23] S. Teng et al., "Motion planning for autonomous driving: The state of the art and future perspectives," *IEEE Trans. Intell. Veh.*, vol. 8, no. 6, pp. 3692–3711, Jun. 2023.
[24] J. F. Medina-Lee, J. Godoy, A. Artuñedo, and J. Villagra, "Speed profile generation strategy for efficient merging of automated vehicles on roundabouts with realistic traffic," *IEEE Trans. Intell. Veh.*, vol. 8, no. 3, pp. 2448–2462, Mar. 2023.
[25] J. Zhang, W. Sun, and H. Jing, "Nonlinear robust control of antilock braking systems assisted by active suspensions for automobile," *IEEE Trans. Control Syst. Technol.*, vol. 27, no. 3, pp. 1352–1359, May 2019.
[26] H. Pan, D. Zhang, W. Sun, and X. Yu, "Event-triggered adaptive asymptotic tracking control of uncertain MIMO nonlinear systems with actuator faults," *IEEE Trans. Cybern.*, vol. 52, no. 9, pp. 8655–8667, Sep. 2022.
[27] H. Pan and W. Sun, "Nonlinear output feedback finite-time control for vehicle active suspension systems," *IEEE Trans. Ind. Inform.*, vol. 15, no. 4, pp. 2073–2082, Apr. 2019.
[28] X. Jing, "The X-structure/mechanism approach to beneficial nonlinear design in engineering," *Appl. Math. Mech.*, vol. 43, pp. 979–1000, 2022.
[29] Z. Wu, X. Jing, J. Bian, F. Li, and R. Allen, "Vibration isolation by exploring bio-inspired structural nonlinearity," *Bioinspiration Biomimetics*, vol. 10, no. 5, 2015, Art. no. 056015.
[30] T. Huang, H. Pan, W. Sun, and H. Gao, "Sine resistance network-based motion planning approach for autonomous electric vehicles in dynamic environments," *IEEE Trans. Transport. Electrific.*, vol. 8, no. 2, pp. 2862–2873, Jun. 2022.
[31] M. Zhang, X. Jing, and G. Wang, "Bioinspired nonlinear dynamics-based adaptive neural network control for vehicle suspension systems with uncertain/unknown dynamics and input delay," *IEEE Trans. Ind. Electron.*, vol. 68, no. 12, pp. 12646–12656, Dec. 2021.

Tenglong Huang received the B.E. degree in automation from the Henan University of Technology, Zhengzhou, China, in 2019. He is currently working toward the Ph.D. degree with the Research Institute of Intelligent Control and Systems, Harbin Institute of Technology, Harbin, China. His research interests include motion planning, vehicle dynamics control, adaptive control, fault-tolerant control, and intelligent vehicles.

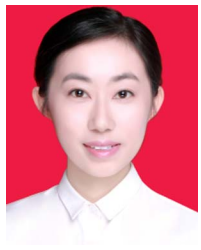

Jue Wang received the B.S. degree in automation and the M.S. degree in pattern recognition and intelligent system from Huaqiao University, Xiamen, China, in 2016 and 2019, respectively. She is currently working toward the Ph.D. degree in control science and engineering with the Research Institute of Intelligent Control and Systems, Harbin Institute of Technology, Harbin, China. Her research interests include adaptive control, fault-tolerant control, and intelligent vehicles.

Huihui Pan (Senior Member, IEEE) received the Ph.D. degree in control science and engineering from the Harbin Institute of Technology, Harbin, China, in 2017, and the Ph.D. degree in mechanical engineering from Hong Kong Polytechnic University, Hong Kong, in 2018. Since December 2017, he has been with the Research Institute of Intelligent Control and Systems, Harbin Institute of Technology. His research interests include nonlinear control, vehicle dynamic control, and intelligent vehicles. Dr. Pan is an Associate Editor for IEEE TRANSACTIONS ON INTELLIGENT VEHICLES and *Mechatronics*.